Improvement of photogrammetric accuracy by modeling and correcting the thermal effect on camera calibration

M. Daakir, Y. Zhou, M Pierrot Deseilligny, C. Thom, O. Martin, E Rupnik

Improvement of photogrammetric accuracy by modeling and correcting the thermal effect on camera calibration

M. Daakir[a,b,*], Y. Zhou[b,c,*], M. Pierrot Deseilligny[b], C. Thom[b], O. Martin[b], E. Rupnik[b]

[a] *SIXENSE Mapping, 1, Rue du docteur Charcot, 91421 Morangis, France*
[b] *Université Paris-Est, IGN, LaSTIG, ACTE, ENSG, 6-8 Avenue Blaise Pascal, 77455 Champs-sur-Marne, France*
[c] *Compagnie Nationale du Rhône, 2 rue André Bonin, 69004 Lyon, France*

Abstract

This paper presents a new method for improving the geometric accuracy of photogrammetric reconstruction by modeling and correcting the thermal effect on camera image sensor. The objective is to verify that when the temperature of image sensor varies during the acquisition, image deformation induced by the temperature change is quantifiable, modelisable and correctable. A temperature sensor integrated in the camera enables the measurement of image sensor temperature at exposure. It is therefore natural and appropriate to take this effect into account and to finally model and correct it after a calibration step. Nowadays, in cartography applications performed with UAV, the frame rate of acquisitions is continuously increasing. A high frame rate over a long acquisition time can result in an important temperature increase of the image sensor and thus introduces image deformations. The correction of the above-mentioned effect can improve the measurement accuracy. We present three methods to calibrate the thermal effect and experiments on two datasets are carried out to verify the improvement in terms of the photogrammetric accuracy.

∗. Corresponding author
Email addresses: mehdi.daakir@sixense-group.com (M. Daakir), yilin.zhou@ensg.eu (Y. Zhou), marc.pierrot-deseilligny@ensg.eu (M. Pierrot Deseilligny), christian.thom@ign.fr (C. Thom), olivier.martin@ign.fr (O. Martin), ewelina.rupnik@ign.fr (E. Rupnik)

Preprint submitted to ISPRS Journal of Photogrammetry and Remote Sensing, 1er janvier 2019

Keywords: photogrammetry ; thermal deformation ; CMOS ; metrology.

1. Introduction

Photogrammetry has undergone an unprecedented evolution in the past two decades. Its simplicity and efficiency make it an accessible and "low-cost" 3D modeling technique. Thus, thanks to its adaptable accuracy, which depends on several parameters, among them the ground sampling distance (GSD), image overlap and network structure, photogrammetry has become a standard technique for contactless metrological applications. Today, photogrammetry benefits from the development of cameras, the ever higher power of computers, the rise of UAV-photogrammetry and the multitude of quasi-automatic software solutions to carry out data processing. However, the use of photogrammetry under metrological conditions requires the total control of physical phenomena, such as : modeling of sensor internal geometry and the condition of image acquisitions. With the continuous development of cameras, nowadays it is possible to obtain a temperature measurement of the sensor at exposure time, which can be used as an accurate indicator of the camera thermal state.

When a camera is subject to a variation of temperature, it undergoes a deformation which impacts the internal parameters. It is recommended to use metric cameras with stable camera internal parameters. The quality of internal geometry modeling impacts directly the photogrammetric accuracy. If the assumption of stable internal parameters is not valid, it is possible, for instance, to perform image-variant calibration. However, this strategy is numerically less stable given the large number of parameters to estimate and strong correlations between internal and external parameters can lead to over-parametrization issues Remondino and Fraser (2006). If the image deformations due to thermal effect are a deterministic function of temperature, and one knows the temperature, it becomes possible to model and eventually correct the introduced systematic effect. In this paper we propose a method for modeling and correcting the thermal effect to improve the photogrammetric accuracy.

The publication is structured as follows. The next section 2 gives a literature review of thermal effect on cameras. Section 3 gives the characteristics of the

utilized sensor. Section 4 presents the model and methods for calibrating the thermal effect. Then, in Section 5 to validate our approach, results obtained with experimental data are shown. Finally, conclusion and potential further work are discussed in sections 6 and 7.

2. Thermal influence on cameras - literature review

Photogrammetric methods have been proved to be particularly useful in engineering where high precision measurements are required (Kölbl (1976), Rieke-Zapp and Nearing (2005), Luhmann (2010)). Multiple factors can have an impact on photogrammetric accuracy. First of all, a higher resolution of images can lead to a higher accuracy because of the increased angular accuracy. Secondly, camera self-calibration can be crucial to determining internal and external parameters of a camera, e.g., focal length, principal point and lens distortion. The quality of camera pose estimation also has an important role in photogrammetric accuracy, and its quality improves as the quality of tie points extraction improves.

Images taken with metric cameras Mcglone et al. (1980) can be exploited for photogrammetric purposes without additional control of inner and relative orientation. Charge-coupled device (CCD) and complementary metal-oxide semiconductor (CMOS) image sensors are commonly used in metric cameras. For low light level applications, an intrinsic noise so called dark current limits the resolution of the CCD sensors (Saks (1980), Widenhorn et al. (2002)). This is due to the fact that electrons can be thermally excited into the conduction band. The generation of dark current is a thermally activated process and as such strongly temperature dependent. Moreover, CCD sensors consume more energy and provide lower frame rate. Therefore, CMOS image sensors have become major players in the solid-state imaging market, a market in which CCD image sensors were once the dominant product. CMOS image sensors utilize an array of active pixel image sensors and can be easily integrated into CMOS process peripheral circuitry since they are made with the same CMOS process technology.

Schwartz (2010) points out that the temperature range of CMOS sensors is quite an improvement compared to that of CCD image sensors. Nonetheless, the temperature change of CMOS image sensors during image acquisitions can still introduce a thermal effect on images. Lin et al. (2010) quantifies the

radiometric effect on a CMOS image sensor, fixed pattern noise is observed to increase with temperature. Sauer (2001) presents a method correcting fixed pattern noise of a CMOS image sensor which can be a result of temperature changes during standard operation.

The influence of temperature on the internal parameters of the camera is a known effect since the appearance of aerial photogrammetry. Hothmer (1958) lists various sources of errors to be considered in the context of aerial mapping. Among the sources it is mentioned that "the effect of temperature can possibly be considerable". Yastikli and Jacobsen (2005) specifies that, during flight conditions, the vertical temperature gradient causes a significant deformation of the camera lens. Investigations carried out with an aerial camera show that the effect of temperature change induces a variation of focal length of 0.5 µm per degree [0.068 pixels] for a Nikor lens of 20 mm [2575 pixels] (Merchant (2006), Merchant (2012)). Merchant adds : "For a flight with a height of 2000m above ground, this (focal length variation) corresponds to a systematic elevation error of 1 m compared to a position determined by GPS". Experience with the Helimap Mapping System highlights the importance of the calibration step in the process pipeline and particularly the stability of the camera calibration Vallet (2007). The various datasets acquired with this system show that the focal length and the principal point are not very stable. These parameters are mainly influenced by the variation of temperature and vibrations. Over a period of one year, the observed variation in focal length is ~30 µm (for a 35 mm lens, value in pixel is not reported) and ~15 µm for principal point. Smith and Cope (2010) presents a study that investigates the influence of temperature on a commercial digital camera. The experiment consists of leaving the camera for several hours in a fridge to lower its internal temperature. The variation observed in the focal length is 1 µm per degree [0.13 pixel] for a 28 mm lens [3590 pixels]. Fiedler and Müller (2013) study the thermal effect on the Kinect sensor. By alternating and combining different states - variation of internal and external temperature, the impact on sensor measurements is proved to be considerable. The distribution of observations show that the increase in temperature can be interpreted as a zoom-in effect.

3. IGN lightweight metric camera

Consumer-grade or professional low payload cameras available on the market and adopted for metrology applications are not strictly metric. To improve the camera mechanical stability, aperture and focus locking screws are often applied Pauly et al. (2017). Alternatively, companies provide cameras said to be optimized for UAV-acquisitions Francois and Yannick (2017). Seldom, research institutions like DLR Kraft et al. (2017) or IGN Martin et al. (2014) manufacture their own camera systems that are able to meet the weight constraints imposed by UAV platforms and the satisfying stability the metric camera demands Kraft et al. (2016).

3.1. Generalities

CamLight – the IGN's metric camera used within this research work – is presented in Figure 1. The camera has been employed in several research applications, e.g. for linear aerial photogrammetric acquisition in the context of DEM restitution of dykes Zhou et al. (2018) ; for metrology with an integrated single-frequency GPS receiver Daakir et al. (2017) ; for online on-chip processing to motion blur caused by erratic UAV movements Audi et al. (2017).

The camera employs a global shutter to avoid the shearing effect and the sensor chip is a monochromatic 20M pixels (5120×3840) CMOSIS CMV20000 that records at up to 30 images per second CMOSIS (2015). Thanks to the integrated GPS chip, a high-precision synchronous GPS/image registration is possible. See Table 1 for a summary of the camera's characteristics.

FIGURE 1: CamLight – the light metric camera for UAV applications developed at IGN.

sensor	
type	CMOS
shutter	electronic : global shutter
spectral range	monochromatic
format	24.5 × 32.7 mm
image format	3840 × 5120 pixels
pixel size	6.4 × 6.4 µm
lens	
focal length	fixed, Leica 35 mm (5489 pixels)

TABLE 1: Characteristics of IGN light camera

3.2. Temperature registration

The CMOSIS CMV20000 chip incorporates a temperature sensor CMOSIS (2013). The temperature measurements are translated to the device temperature with the help of Eq. (1).

$$\text{Register value}[\text{DN}] = \text{gradient}[\frac{\text{DN}}{^\circ C}] \times \text{Temperature}[^\circ C] + \text{Offset}[\text{DN}] \quad (1)$$

where DN is the digital number, Offset is the value of the register at $0^\circ C$. Typical values of the gradient and the offset are given by the manufacturer. The temperature recorded is quite close to the absolute temperature as we use typical calibration values offered by constructors. However, these parameters vary slightly from recorders and need to be recalibrate when the absolute temperature is required. In our research, we are only interested in the variation of the temperature.

Note that the measured image sensor temperature does not fully represent the thermic state of the camera. Temperature of the external environment has equally an impact on the camera's internal parameters Pan et al. (2015). Within this work we do not discuss the influence of the external temperature, nonetheless, during the experiments we kept the variation of the environment temperature as low as possible by, (i) for the indoor case, conducing it in a space of constant temperature, and (ii) for the outdoor case, conducting it in a short period of time.

4. Calibration of thermal effect

The adopted thermal model and two evaluation methods are presented below. Both methods infer the sensor's response to the raising temperatures via the changing focal length (i.e. scale factor), translation and rotation of the image. The first evaluation method relies on the image correlation technique, whereas the second estimates the parameters in a bundle adjustment routine.

Hypothesis. In this section, we seek to determine the variation of the camera interior orientation according to the variation of the temperature. It is not possible to precisely determine the interior orientation parameters from a single image (4.3.1), nor from a pair of images taken from the same point of view (4.2). Nevertheless, the variation of the interior orientation parameters can be unambiguously determined under the assumption that the camera exterior orientation parameters remain unchanged.

4.1. Thermal model

The thermal effect has an impact on the camera internal parameters and manifests in 2D displacements of the image pixels. We model the induced displacement with a 4-parameter 2D spatial similarity transformation (cf. Eq. 2). The choice of the model was driven by its simplicity of interpretation. It models the effect of the changing focal length and small rotations therefore allows for physical understanding of the arising deformations. In practice, generic polynomials ensure much finer modeling hence shall be preferred (cf. Eq. 3).

$$\begin{bmatrix} i_C \\ j_C \end{bmatrix} = \begin{bmatrix} u(T) \\ v(T) \end{bmatrix} + k(T) \begin{bmatrix} cos(\theta(T)) & -sin(\theta(T)) \\ sin(\theta(T)) & cos(\theta(T)) \end{bmatrix} \times \begin{bmatrix} i_R \\ j_R \end{bmatrix} \tag{2}$$

where : T = temperature of the camera ;
$[i_C, j_C]^t$ = corrected image coordinates ;
$[u(T), v(T)]^t$ = vector of translation ;
$k(T)$ = scale factor ;
$\theta(T)$ = angle of rotation ;
$[i_R, j_R]^t$ = original image coordinates.

The parameters are estimated with the least squares solver. All pixels of the deformation map computed with image correlation technique (see 4.2) are

used as observation.

We assume the thermal effect to be a deterministic function of temperature. For one image taken under a given temperature T, the deformation $\mathscr{M}_{T_0}^{T}(x, y)$ that the thermal effect introduces with respect to the image of reference taken under T_0 is computed. As we cannot compute $\mathscr{M}_{T_0}^{T}(x, y)$ for all values of T, we estimate a deformation model from a set of computed deformations $(\mathscr{M}_{T_0}^{T_1}, \mathscr{M}_{T_0}^{T_2}, \cdots, \mathscr{M}_{T_0}^{T_N})$. The estimated deformation model is presented in Eq. (3).

$$\mathscr{M}_{T_0}^{T}(x, y) = \sum_{k=1}^{3} \sum_{i=1}^{4} \sum_{j=1}^{4} a_{k,i,j} T^k x^i y^j \tag{3}$$

All image pixels are used as observation for the coefficient determination of the said model. Therefore, even if the degree of freedom is quite high, there is no risk of over-parametrization. Once the deformation function is computed, to remove the deformation for any value of T, a correction function is interpolated. Tie points, and GCP (Ground Control Point) image measurements are subsequently corrected as shown in the processing workflow in Fig. 2.

4.2. Deformation determination by 2D image correlation

4.2.1. Parametrization

2D sub-pixel image correlation implemented in Pierrot-Deseilligny and Paparoditis (2006) is used as the deformation measurement technique. Correlation is a well-established method for determining 2D displacement maps in the field of Earth Sciences (Rosu et al., 2015) and in industrial applications Maas and Hampel (2006).

Our camera is static during the experiments, therefore, any displacement in image space corresponds to the effect of the sensor's temperature variation. Among the essential correlation parameters there are : searching interval (SI), discretization step (DS), correlation threshold (CT), correlation weight (CW), number of exploited directions (DIR) and the correlation window size (CWS). The SI defines the displacement search area, the DS is the sub-pixels precision, the CT is the value below which two pixels will be regarded as not correlated, the CW is a weight that increases the significance of the better-correlating pixels within the optimization, and the DIR corresponds to the number of direction exploited in optimization phase. The parameter values

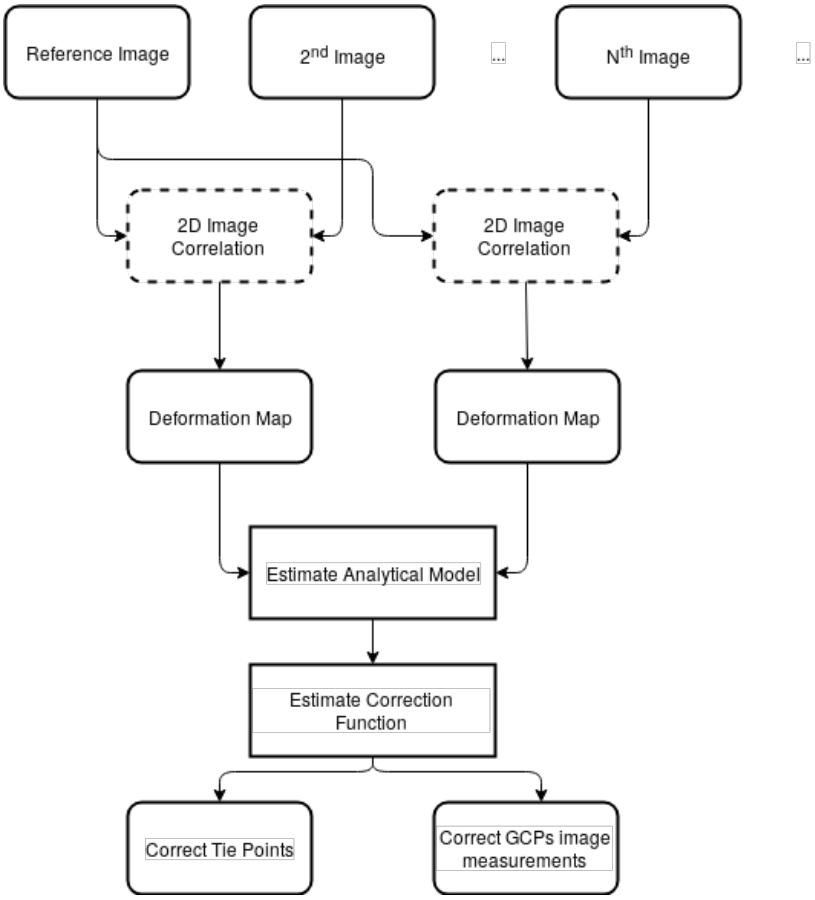

FIGURE 2: General workflow for thermal deformation modeling.

should be adapted to the nature of the anticipated displacements. Here, as the thermal effect causes 2D low amplitude movements, it turns out that parameters similar to those defined in Rosu et al. (2015) for analyzing seismic events were adequate. The reader is referred to this publication for more detailed understanding of the individual parameters as well as to Hirschmuller (2008) regarding the correlation optimization scheme. See Tab. 2 for the list of parameters and their values.

4.2.2. Experiment design

Two cameras fixed on one heavy tripod observe a textured wall and perform two independent acquisitions (see Fig. 3). The objective on the one hand is to collect wide range of temperature scenarios so as to provide a complete

Parameter	Value
Searching interval (px)	6
Discretization (px)	0.2
Correlation Threshold	0.5
Weight of correlation	2
Number of directions	7
Size of window	20

TABLE 2: Selected parameters for the correlator

temperature correction model. On the other hand, we want to verify that the deformations are repeatable for similar temperature scenarios. Type I acquisition consists of taking image sequences from the same point of view as
220 the camera temperature increases. Type II acquisition uses a second camera with a cooling system attached to its back. The cooling system is a Peltier solid-state active heat pump which transfers heat from one side of the device to the other[1]. Tab. 3 presents details on the realized acquisitions, Fig. 5 depicts the temperature variation.

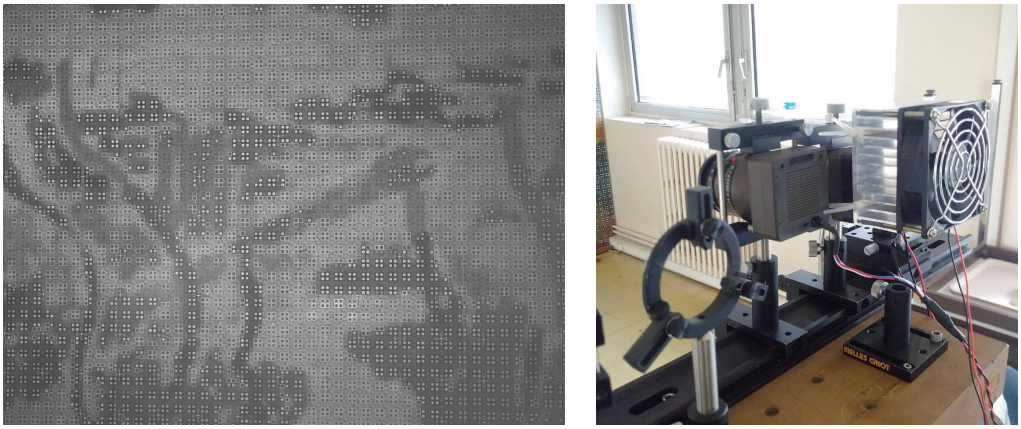

FIGURE 3: The scene of the textured wall (left) and the installation of cameras and Peltier cooler (right).

1. https://en.wikipedia.org/wiki/Thermoelectric_cooling

Type I acquisitions. Three acquisitions are performed. The first two are acquired successively on the same day with the temperature rounding to an integer ; the third acquisition is obtained on another day with the temperature rounding to an increment of 0.3°C or 0.4°C. This setting is to study the influence of temperature precision on the quality of maps and to ensure that the deformation is stable over time. The frame rate is set to approximately one image every 4 seconds to get a significant increase of the camera temperature.

For each acquisition, the first image is considered as the image of reference. Deformation maps are generated by comparing each successive image with the reference.
Fig. 4 shows an example of the correlation map being an indicator of the matching quality between images and an example of a deformation map.

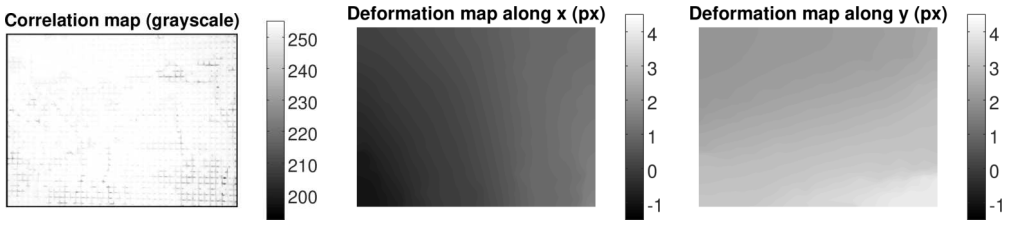

FIGURE 4: An example of the correlation map (left) and the 2D deformation map along x (center) and y axis (right)

Type II acquisition. The acquisition frame rate is decreased to one image per minute. With the cooling effect behind, the camera temperature varies within a small range. The temperature is rounded to an increment of 0.3°C or 0.4°C. Here, to verify the absence of deformation when there is no change on the camera temperature, two image couples taken under the same temperature with a long time interval are considered. Tab. 4 provides details on the investigated image couples.

4.2.3. Results

Type I acquisition. The parameters (translations, rotation and the scale factor) of the 2D spatial similarity transformation that model the induced

	Type	Acquisition time (min)	Nb of images	Temperature range (°C)
Dataset 1	I	38	597	$[24, 49]$
Dataset 2	I	44	716	$[25, 50]$
Dataset 3	I	30	377	$[24.8, 56.2]$
Dataset 4	II	37	37	$[22.9, 23.6]$

TABLE 3: Information of 2D correlation datasets

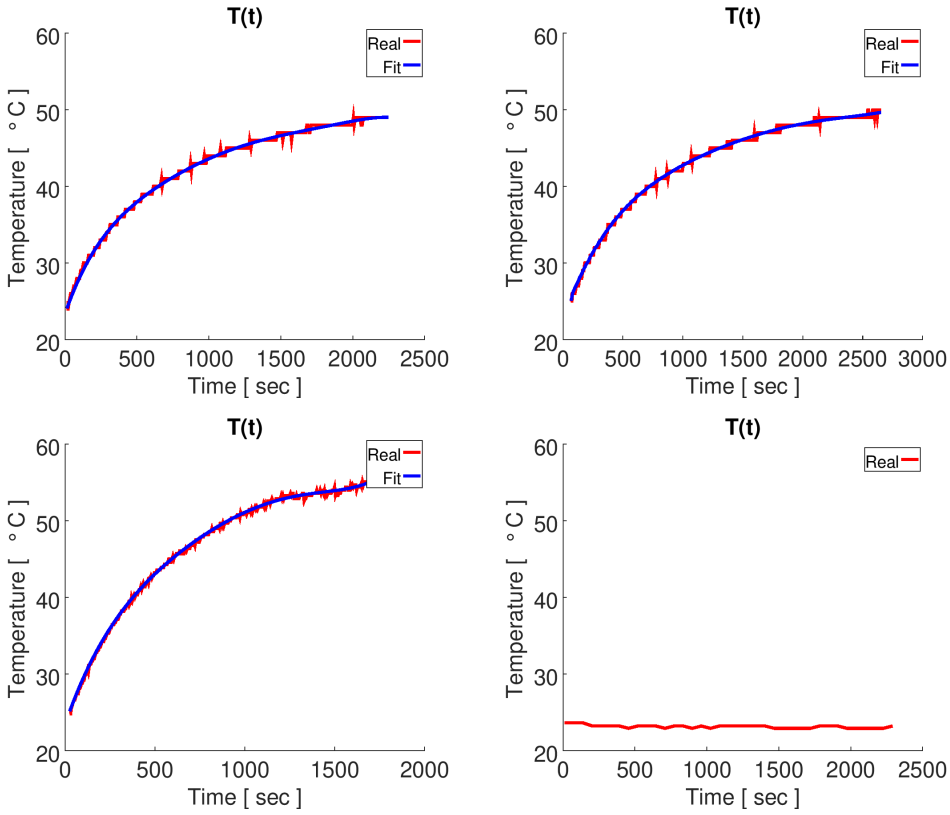

FIGURE 5: Temperature variation in Type I acquisition : dataset 1-3. Temperature variation in Type II acquisition : dataset 4 (lower right)

250 deformations is presented in Figs. 6-8. The focal length depicted is the estimated mean scaling factor on all image pixels. All parameters increase with the temperature. The variation of the translation corresponds to the deviation of the principal point. The variation of the focal length and the rotation can

	Temperature (°C)	Time interval (min)
Couple 1	22.9	29
Couple 2	23.2	28

TABLE 4: The investigated image couples in Type II acquisition.

be interpreted as image sensor deformation caused by component dilatation. For dataset 1 and dataset 2 acquired on the same day, all the 4 parameters vary in the same way and a good repeatability of the thermal effect is observed. Dataset 3, acquired 4 months later, has a similar focal length variation, whereas the variation of translation and rotation differ from dataset 1 and 2. For all 3 datasets, the variation of rotation remains insignificant during the acquisition (less than 0.02 px/°C). The thermal effect is reproducible but not repeatable over time for all parameters. We are not yet able to explain why translation varies differently over time. To be mentioned, the slope of the focal length variation 0.4-0.5 µm per degree [0.07-0.08 px/°C] is of the same scale as the result presented in Merchant (2012, 2006) 0.5 µm per degree [0.068 px/°C)].

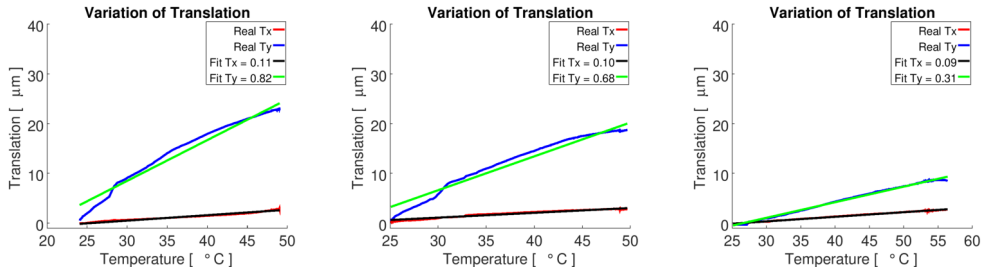

FIGURE 6: Estimated translation : dataset 1-3 (from left to right). T_x and T_y are the translations along respective axes.

Type II acquisition. The sensor temperature barely changes during the experiment. Consequently, the acquisition serves to quantify the impact of unidentified and uncontrolled effects of the sensor deformations, e.g. the ambient humidity or ambient temperature. The 2D deformation maps calculated for image couples are homogeneous across the image plane and demonstrate

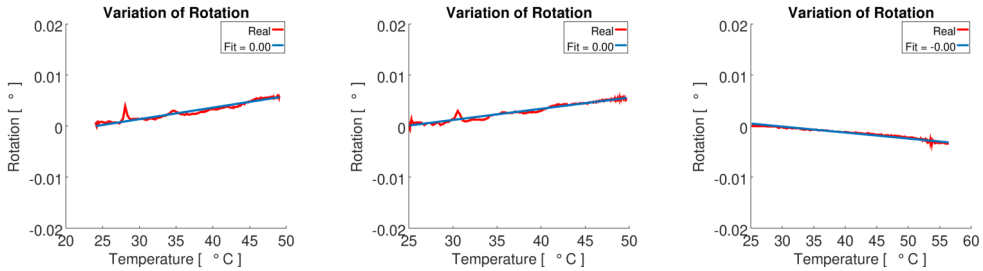

FIGURE 7: Estimated rotation : dataset 1-3 (from left to right).

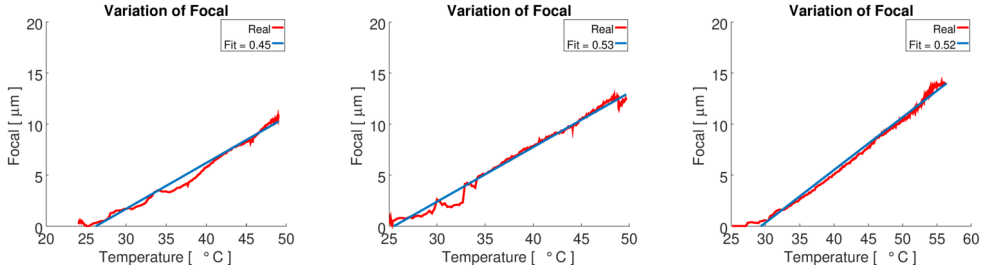

FIGURE 8: Estimated focal length : dataset 1-3 (from left to right).

no displacements along the x,y axes (cf. Fig. 9 and Tab. 5). The result justifies that external factors have negligible effect and the observed deformation within type I acquisition is the sensor's response to the raising internal temperature.

	min (px)	max (px)	mean (px)	std (px)
Axis X Couple 1	-0.04	0	-0.01	0.01
Axis Y Couple 1	0	0	0	0
Axis X Couple 2	-0.04	0.04	-0.01	0.02
Axis Y Couple 2	0	0	0	0

TABLE 5: Deformation computed for two image couples in type II acquisition.

4.3. Deformation determination with bundle adjustment

To confirm our previous findings, two independent acquisitions and evaluation methods using the space resection algorithm and the bundle adjustment

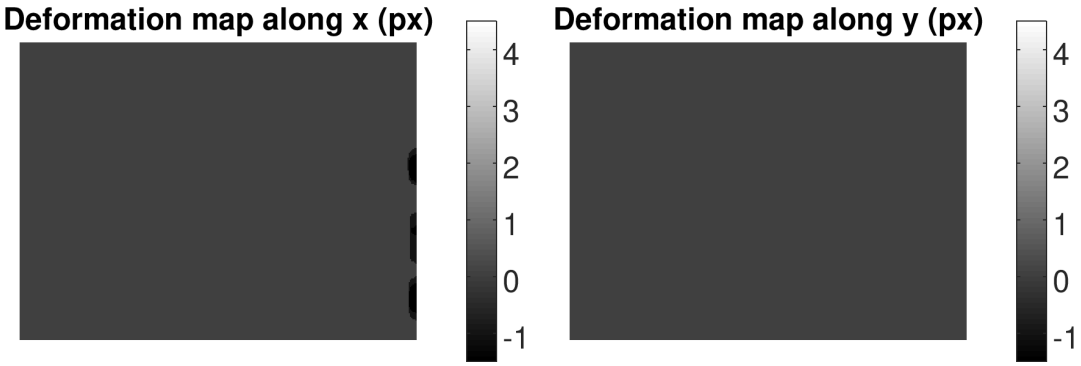

FIGURE 9: Example of deformation maps calculated along x and y in type II acquisition.

were conducted. During the first acquisition the camera is static and observes a calibration field with GCPs surveyed with a total station and distributed along three dimensions (cf. Fig 10). During the second acquisition, a number of convergent images around the same GCP field are taken. The results are interpreted in terms of the changing focal length and the principal point. The bundle adjustment method adopts the perspective projection model, see Eq. (4).

$$I_l = \zeta(\pi(R_i(P_l - C_i))) \tag{4}$$

where : $I_l = 2d$ image position of GCP point l on image i (observation) ;
$\zeta = \mathbb{R}^2 \rightarrow \mathbb{R}^2$ transformation describing the camera model
$\pi = \mathbb{R}^3 \rightarrow \mathbb{R}^2$ perspective projection ;
(R_i, C_i) = pose of image i ;
$P_l = 3d$ position of GCP l on image i (observation).

4.3.1. Static camera

In this section, a second experiment is carried out independently from the 2D image correlation (section 4.2) to confirm the variation of calibration parameters over temperature change.

The camera is fixed on a heavy tripod to ensure its stability during the acquisition and its temperature raises progressively (cf. Fig.10). The camera poses of a pre-calibrated camera (camera model Fraser (1997)) are firstly recovered with the space resection algorithm using all GCPs. Then, a bundle

adjustment is performed where the previously computed poses are considered constant, and solely the focal and the principal point are considered unknown. The GCP image measurements were done manually in the first image. For subsequent images automated cross correlation with respect to the first image was computed. See Tab. 6 for information on temperature ranges, the calibration field and GSD.

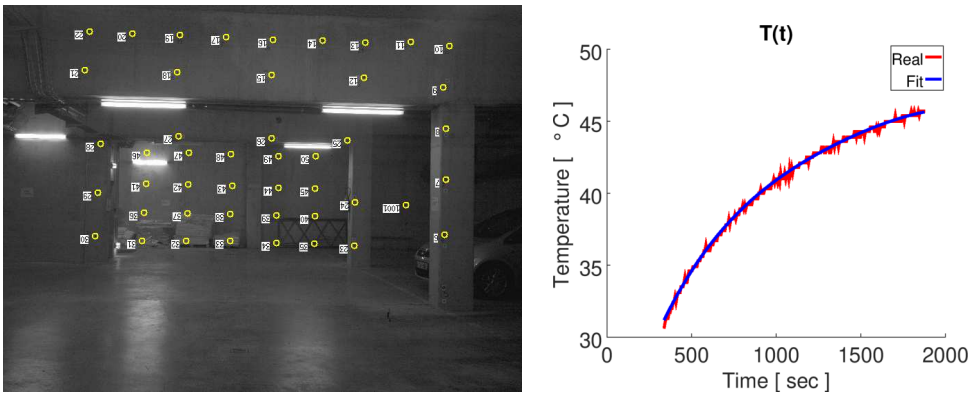

FIGURE 10: The calibration field with GCPs (left) and temperature variation (right)

Acquisition time (min)	26
Number of images	263
Temperature range (°C)	[30.6,45.7]
Mean Nb of GCPs / image	21
GSD range (mm)	[1.6,4.0]
DOF Topometric Network	488
Mean GCP accuracy (mm)	1.7

TABLE 6: The static camera dataset.

Results. Figure 11 shows the reprojection error for each GCP. The red curve depicts the GCP reprojection error of the first image and gives an indication of the pose estimation quality. The blue curve shows the average GCP reprojection error by estimating a focal length and a principal point per image.

The reprojection error of the first image has an average of 0.57 px and a dispersion of 0.34 px while for the mean reprojection error, the average is of 0.16 px and the dispersion of 0.07 px. Small residuals indicate an accurate pose estimation and justify the imposition of the first image camera pose on other images. The estimation of the focal length and the principal point for images is therefore considered reliable.

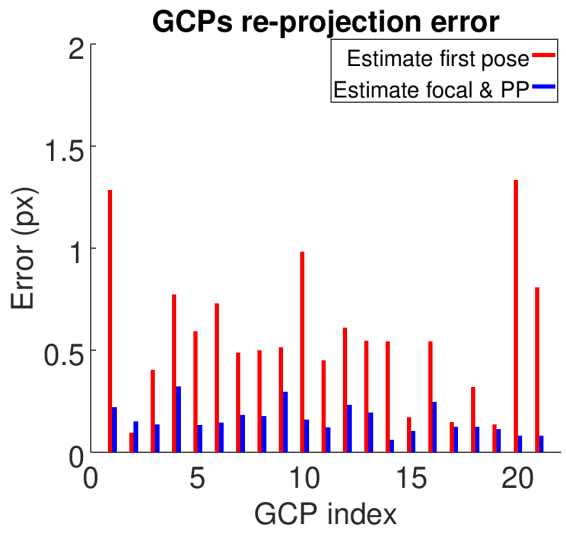

FIGURE 11: GCP reprojection error of the first image and mean GCP reprojection error of all images; x-axis represents the GCP index

Figure 12 shows the variation of the focal length and the principal point with temperature. The variation of the focal length is coherent with the results obtained in Section 4.2 but the planimetric trend of the principal point does not correspond to the translation parameters. This is partly due to the fact that acquisitions spread over a long time. With this, however, one can conclude that the thermal deformation can be modeled and is reproducible at least for focal length.

4.3.2. Moving camera

A multi-view convergent imaging network is acquired in this experiment (cf. Fig. 13). Three experiments with three different temperature ranges were

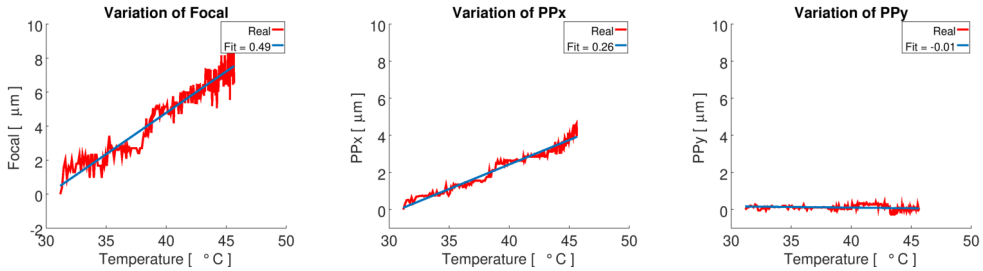

FIGURE 12: Evolution of estimated focal length and principal point values.

performed. The images are taken within a very short period of time to guarantee a stable temperature condition. Unlike the static camera case (section 4.3.1), the imaging geometry allows us to simultaneously estimate both the poses and the internal calibrations for each image (i.e. the focal length and the principal point). Among the three datasets (cf. Tab. 7), the temperature variation of the first dataset is more important since the temperature increases more rapidly when the temperature is low.

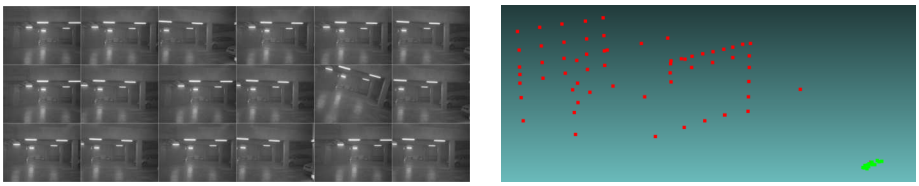

FIGURE 13: The acquired images (left) and their poses (right). Camera positions are in green and the GCPs in red.

	Dataset 1	Dataset 2	Dataset 3
Number of images	14	16	18
Temperature range (°C)	[25.2,29.5]	[39.2,39.6]	[45.4,45.7]
Mean temperature (°C)	27.6	39.3	45.5
GSD range (mm)	[1.6,4.0]		
DOF Topometric Network	488		
Mean GCP accuracy (mm)	1.7		

TABLE 7: The moving camera dataset.

Results. For each experiment we estimate one camera model. Fig. 14 presents the average reprojection error for each GCP, Tab. 8 contains both GCP residuals and the estimated camera internal parameters, and Fig. 15 shows the variation of estimated parameters over temperature. One can see an increasing tendency of the GCP reprojection error with the increasing GCP index for all three experiments. In fact, GCPs with larger indexes locate further away from the camera ; these GCPs have therefore higher GSD and thus less favourable image measurement precision.

Ideally, this experiment shall be supplemented by datasets at low temperature values. Nevertheless, the rapid change of temperature at low value prohibited us from carrying out experiments for other temperature ranges.

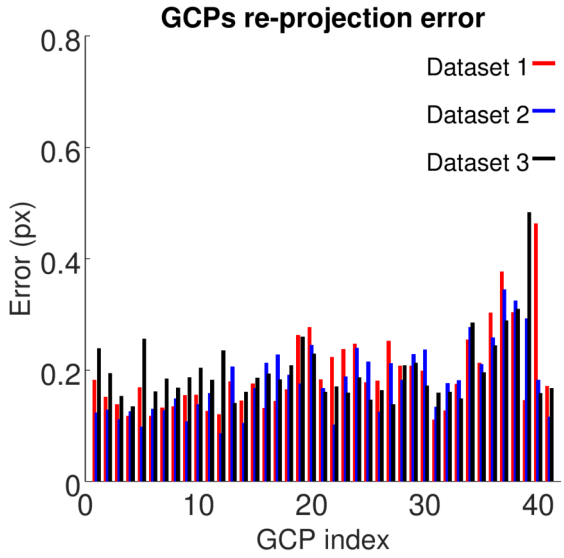

FIGURE 14: GCP reprojection error ; x-axis represents the GCP index

5. Experimental evaluation

The thermal model estimated in the previous section is here applied to two real-case studies, terrestrial and airborne (cf. Sections 5.1, 5.2). The mean absolute residual on GCPs and a loop closing error were the measures adopted to evaluate the precision of respective experiments. The goal was to demonstrate how good a photogrammetric restitution can be without the inclusion

	Datatset 1	Datatset 2	Datatset 3
mean (px)	0.19	0.18	0.20
std (px)	0.07	0.06	0.06
f (px)	5506.02±0.5	5506.16±0.6	5507.59±0.5
PP_x (px)	2528.49±0.5	2529.40±0.5	2527.27±0.4
PP_y (px)	1931.64±0.5	1933.90±1.1	1936.56±0.8

TABLE 8: GCP reprojection error and estimated focal length and principal point

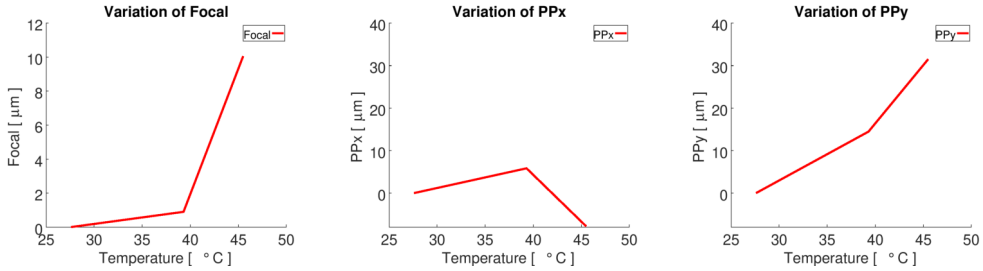

FIGURE 15: Estimated values of focal length and principal point.

of GCPs in the processing. Accordingly, the relative result was moved to the coordinate system of GCPs with a 7-parameter 3D similarity transformation and no bundle block adjustment was followed. As a further consequence, the weight of GCPs is not discussed thereafter. Note that even though for some experiments the accuracy of GCPs is of the same order as the image GSD, one can still draw conclusion on the internal accuracy. Fig. 16 presents the processing workflow.

5.1. Terrestrial acquisition

The dataset is composed of a sequence of images of raising temperature taken around a pylon (cf. Fig. 17). Convergent images and images rotated by 90° were taken. The first and last image pairs were taken from the same viewpoint forming a closed acquisition loop.

The camera relative orientations are calculated in a self-calibrating bundle block adjustment using only SIFT tie points as observations. The camera calibration model combines two high degree polynomial function as discussed

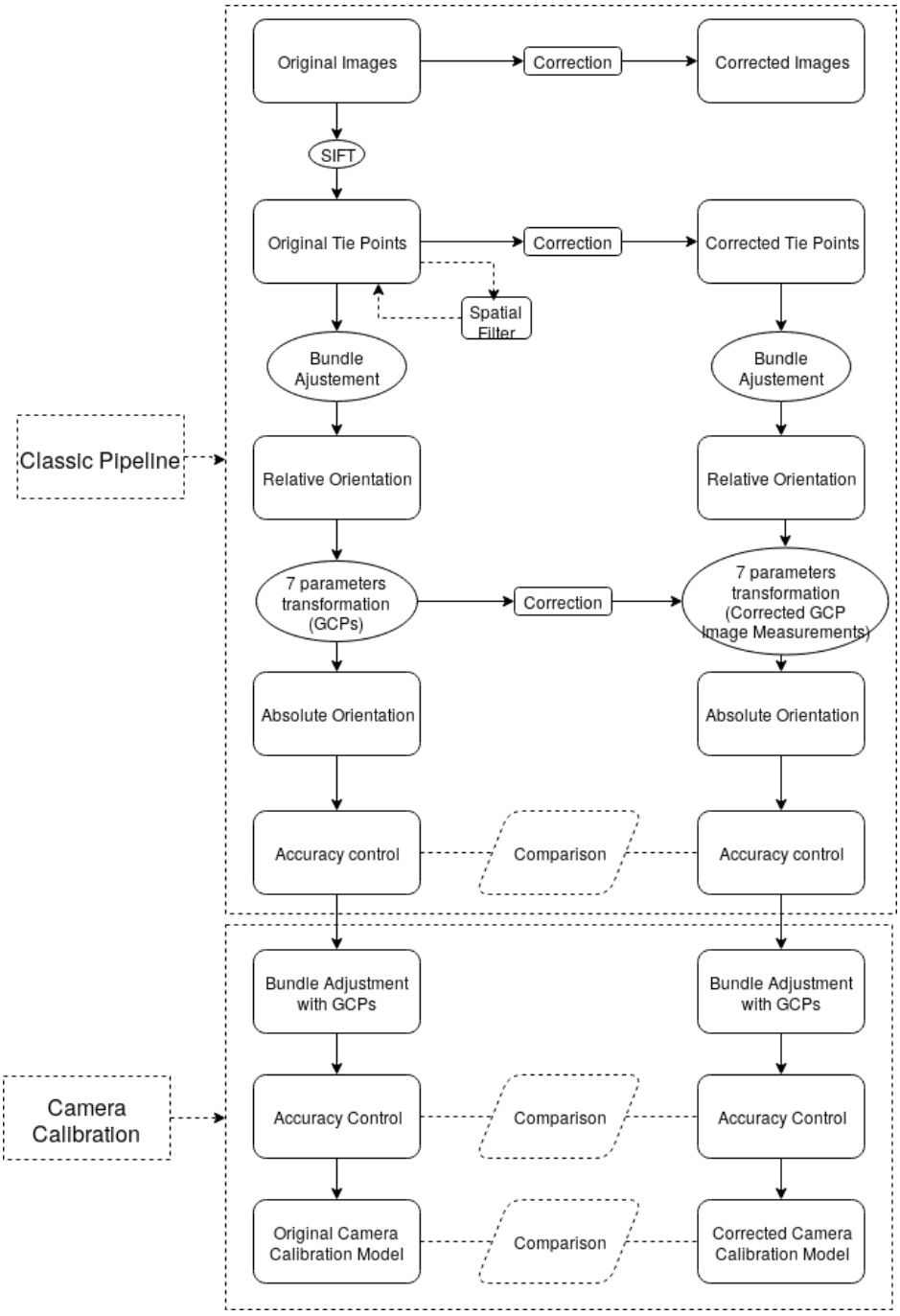

FIGURE 16: Processing workflow. Tie points extraction was carried out with SIFT Lowe (2004).

in Tournadre (2015).

The scene is equipped with a network of GCPs measured with a total station (cf. Tab. 10). Six stations were employed to avoid grazing angle measurements and each target is visible from at least 4 stations. The stations were installed with a "forced centering" strategy to overcome the centering errors. To avoid the height measurement errors, the survey is completed in a free station mode. The measurements are adjusted in Comp3D – a geodetic adjustment software developed at IGN.

The GCPs are exploited in both two presented experiments for relative to absolute transformation. Nonetheless, to evaluate the results, GPCs are used only in the **with closed loop** case in Section 5.1.1. In Section 5.1.2, a GCP-free evaluation is performed in the **without closed loop** scenario.

At all instances, the results corrected for the thermal effect are compared with the results based on original images. To avoid the increase of the computation time, corrections are not applied on the totality of pixels but on tie points and GCP image observations.

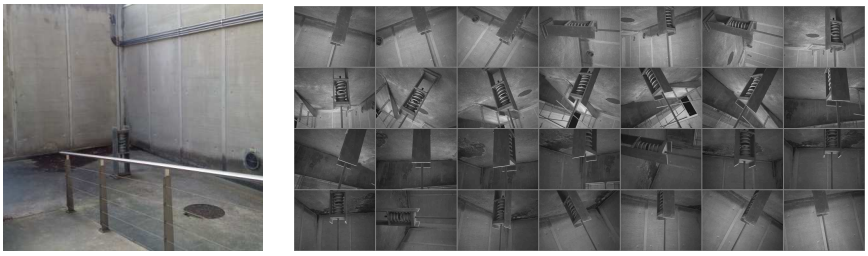

FIGURE 17: The pylon 3D scene (right), and the set of acquired images (left)

Number of images	28
Number of GCPs	13
Acquisition time (min)	14
Temperature range (°C)	[23,31]
GSD range (mm)	[0.5,1.5]

TABLE 9: Information on terrestrial dataset

Horizontal angle uncertainty	5.4 x 10^{-4} °
Vertical angle uncertainty	5.4 x 10^{-4} °
Distance uncertainty	1 mm
DOF of Topometric Network	111
Mean GCP accuracy (mm)	0.3

TABLE 10: Specifications of the total station

Correction ($\surd$ or ×)	Original dataset	Corrected dataset
Images	×	×
Tie points	×	$\surd$
GCPs image measurements	×	$\surd$

TABLE 11: the original and corrected datasets in the terrestrial experiment

For original dataset, tie points are extracted with algorithm SIFT and image measurements are based on original images. For thermal effect corrected dataset, tie points and GCPs image measurements are all generated by applying a correction on original tie point coordinates and original image measurements of GCPs, respectively. The generation of corrected tie points has a significant advantage of being fast and resulting in higher photogrammetric accuracy compared to recomputing tie points on corrected images.

5.1.1. ***Results on GCPs with closed loop***

Three correction maps are applied to the acquired dataset, as presented in Section 4.2. The geometry of the acquisition is shown in Fig. 18, the GCPs residuals are presented in Fig. 19 and Tab. 12.

The order of the GCP residual is relatively high compared to the GSD size. It is due to the fact that no bundle block adjustment was preformed after the 7-parameter 3d similarity transformation. One can observe, however, that the relative accuracy is increasing when thermal corrections are introduced (i.e., compare results of the original dataset with those of the three corrected datasets). Out of the three correction strategies, the **Correction 3** brings the highest precision gain and relates to the highest temperature measurement precision, as explained in Section 4.2. All in all, with the adopted methodology and for similar acquisitions, an accuracy improvement of a factor of 1.5

can be anticipated.

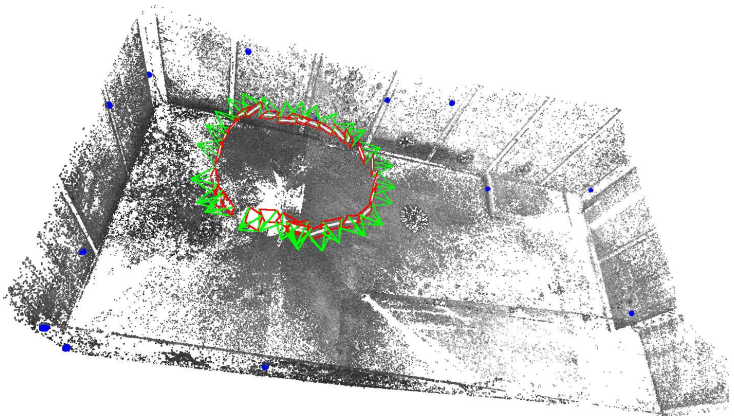

FIGURE 18: Geometry of terrestrial photogrammetric acquisition with GCPs (blue)

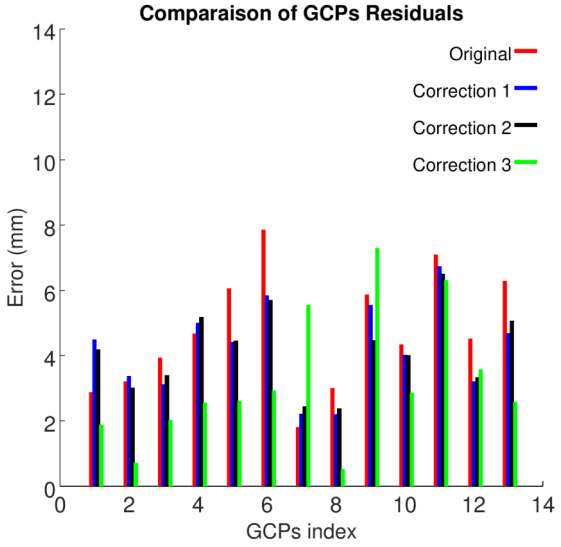

FIGURE 19: Residuals on GCPs.

5.1.2. ***Results without closed loop***

The same set of images is used in this experiment but the dataset is processed as an open loop (cf. Fig. 20). That is, the first and the last pair of images

	min (mm)	max (mm)	mean (mm)	std (mm)
Original	1.8	7.9	4.7	1.8
Correction 1	2.2	6.7	4.2	1.4
Correction 2	2.4	6.5	4.2	1.3
Correction 3	0.5	7.3	3.2	2.0

TABLE 12: Residuals on GCPs after the 7-parameters transformation.

within the acquisition observe the same scene but no tie points relate them. Topologically speaking, it is a linear acquisition. Such image configuration is unfavourable and causes the so-called *bending effect* (James and Robson (2014), Nocerino et al. (2014)). In this experiment we investigate to what extent thermal correction can mitigate this phenomenon.

The closing error explained in Fig. 20 is calculated using the **Correction 3** strategy (cf. Fig.19 and Section 4.2). Tie points extracted from the first and the last two images (4 images in total) are triangulated respectively with observations of the first and the last image pair to obtain two sets of 3D positions. The closing error corresponds to the distances between these two sets of 3D points. In case of no drift, the distances should be close to zeros. See Tab. 20 for the closing error min, max, mean and standard deviation values, as well as Fig. 21 for the closing errors' distribution across the tie points commonly seen by the four images. The closing error declines by a factor ≈ 3.5 when the thermal corrections are applied. Consequently, the *bending effect* is reduced and a better internal accuracy is obtained.

	min (mm)	max (mm)	mean (mm)	std (mm)
Original	1.4	19.8	6.2	2.1
Correction 3	0.0	13.9	1.7	1.6

TABLE 13: Statistics of the closing error.

5.2. Airborne acquisition

The dataset is composed of a 2-strip drone flight along a 500 m road. The objective of this experiment is to investigate the accuracy gain when performing the thermal effect correction in a cartographic application where accuracy expectations are often very stringent. The acquired images, the imaging

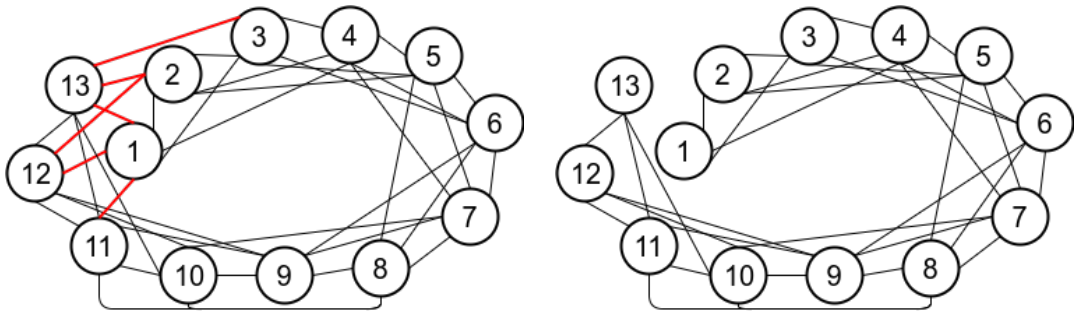

FIGURE 20: Image connectivity graph for standard configuration with closed loop (left). Red lines depict connectivities removed in configuration without closed loop; Image connectivity graph for configuration without closed loop (right). The closing error is calculated on tie points of images 1-2-12-13.

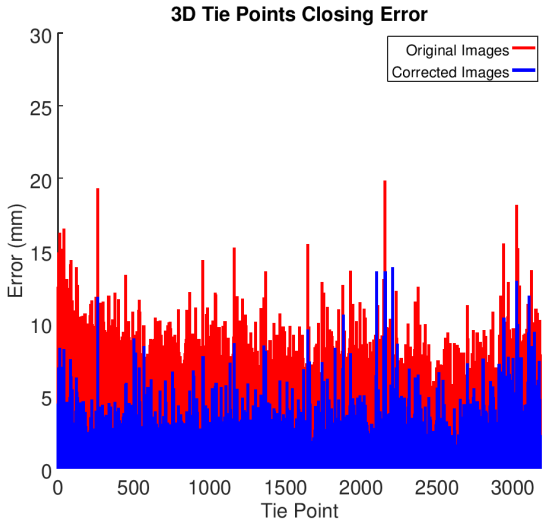

FIGURE 21: Closing error distribution across all tie points.

435 geometry and further flight characteristics are given in Fig. 25, Fig. 26 and Tab. 15, respectively.

As a linear acquisition geometry is unfavourable for self-calibrating purposes, we pre-calibrated the camera by performing a terrestrial acquisition. Two ca-
440 mera models are estimated with original observations and the thermal effect

corrected observations, respectively.

During a drone survey, the temperature changes can stem from various factors, e.g., the sun, the wind, the internal heating of the camera. In this experiment, however, we interest in the camera temperature change itself regardless of the source.

5.2.1. Camera pre-calibration

The terrestrial calibration field contains a number of GCPs and represents a 3-dimensional scene. The camera internal and external parameters are estimated in a self-calibrating bundle block adjustment with tie points and GCPs. See Fig 22 and Tab. 14 for more information on the calibration field and the acquisition itself.

Two calibration models are established – with and without the thermal effect being corrected. The temperature change, despite being small, has an impact on the camera calibration, and subsequently on the geometric accuracy of the drone survey. Both calibration estimated models can be compared as follows :

$$d(\zeta, \zeta') = \min_{\mathscr{R}} \iint \|\zeta - \mathscr{R} \cdot \zeta'\|^2 dxdy \tag{5}$$

where : ζ estimated internal model with original observations ;
ζ' estimated internal model with corrected observations ;
$\mathscr{R}$ estimated rotation

Number of images	43
Temperature range (°C)	[34.2,36]
Number of GCPs	28
GSD range (mm)	[0.5,1.5]
Mean GCP accuracy (mm)	0.5

TABLE 14: Pre-calibration acquisition data and accuracy measures.

Results. The processing strategy follows the scheme as given in Section 5.1. See Fig. 23 for the geometry of the acquisition and the image residuals of GCPs.

FIGURE 22: Images of the calibration field (left). The terrestrial calibration field used for pre-calibrating the camera (right).

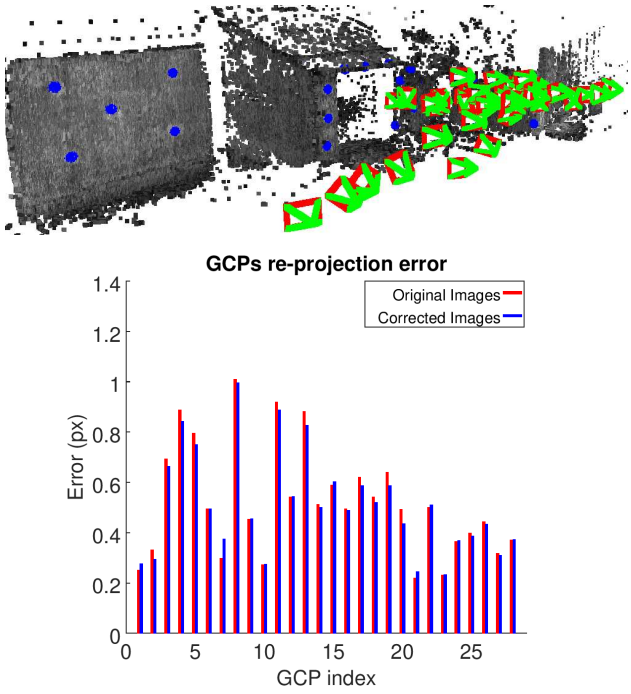

FIGURE 23: Geometry of acquisition for camera model calibration and GCP distribution (top), mean GCPs reprojection error (bottom)

We note that for an identical processing, taking into account the temperature effect gives a slightly better GCP reprojection error statistics, even if the impact is almost negligible. This is explained by the fact that, the variation of temperature is almost insignificant (1.6°C) and the GCP reprojection errors is rather dominated by GCP image measurements. Comparison between the the two camera models estimated with and without thermal effect correction on observations is shown in Fig 24.

With Fig. 24 one can read that the temperature introduces a bias of 0.05 px, displacements of up to 0.33 px are observed at the image borders. The mean deviation on the whole image sensor is 0.23 px.

Despite the small change of camera temperature (1.6°C), the impact on the estimated camera model is measurable. Nevertheless, the interpretation of these changes in terms of 3D photogrammetric accuracy can be tricky. In this case, an independent aerial acquisition is carried out with the two estimated camera models being served for camera pre-calibration (cf. 5.2.2).

5.2.2. UAV acquisition

No measurements of the external temperature during the flight were available. Nonetheless, the variations were minimized by low-altitude flight (70m), short flight duration (15mins) and low speed (2m/s). The GCPs were measured using GNSS RTK surveying, and the evaluation is carried out on GCPs, after having transformed the relative result to the coordinate system of GCPs. Concerning the camera model, the two pre-calibrated camera models discussed above were used in the processing.

Results. Fig. 27 and Tab. 16 report on individual GCP residuals, as well as their statistics for both original and corrected images. There is a clear residual decreasing tendency for most of the GCPs. The results prove that an accuracy improvement of a factor of ~ 1.4 can be anticipated for similar imaging conditions.

6. Conclusion

This article presents different strategies for studying the thermal deformation on images due to the image sensor temperature variation. To our best

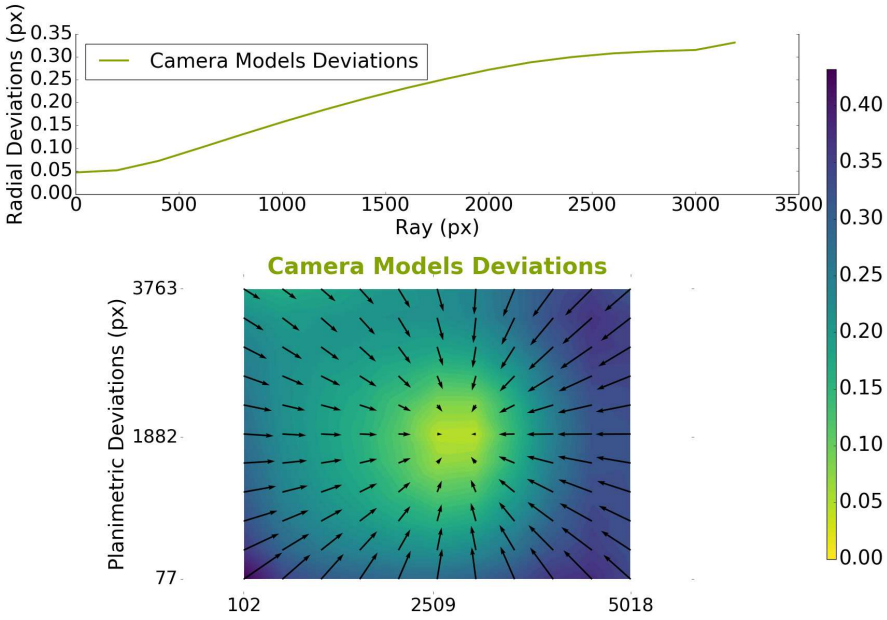

FIGURE 24: Comparison of the two estimated internal camera models

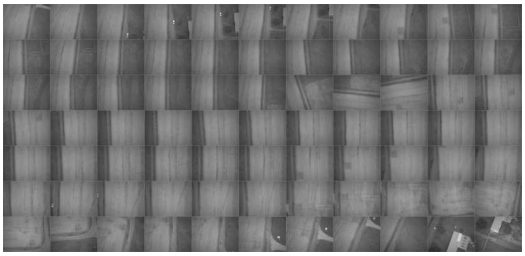

FIGURE 25: Images acquired within the drone experiment.

knowledge, this is the first time the issue of thermal deformation is studied in the context of light weight metric camera devoted to UAV photogrammetric acquisitions.

500 Two modeling techniques were investigated – relying on the image correlation technique, and using a bundle adjustment routine. In either scenario the

Temperature range (°C)	[22.7,28.8]
Flight time (min)	15
Number of images	77
Number of GCPs	10
Flight height (m)	70
GSD (cm)	1
GCP accuracy (cm)	1
Overlap	75%,75%

TABLE 15: UAV acquisition data and accuracy measures.

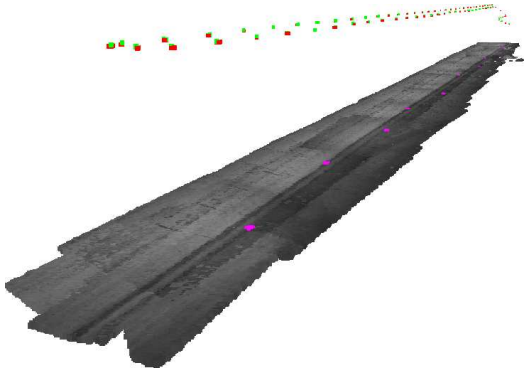

FIGURE 26: Geometry of UAV acquisition and distribution of GCPs (in purple) along the trajectory.

	min (mm)	max (mm)	mean (mm)	std (mm)
Original images	5.9	39.6	21.4	11.0
Corrected images	5.9	24.9	15.5	6.6

TABLE 16: Residuals on GCPs fo the UAV experiment.

sensor's response to temperature is interpreted in terms of the changing focal length, as well as the translation and the rotation of the image.

505 The image matching experiment proves that the thermal deformation has an impact on internal camera parameters (e.g., focal length, principal point) and that the image sensor temperature change is the main cause. This method for quantifying the deformation is complete and exhaustive since it allows

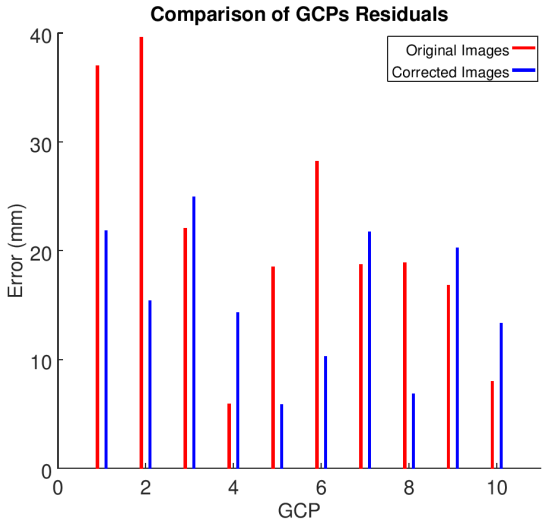

FIGURE 27: Residual distribution on GCPs after the 7-parameter 3D similarity transformation for both original and corrected images.

to study the deformation for every pixel of the image sensor. A good repeatability over time of the focal length variation (0.4-0.5 µm /°C) is observed and the variation corresponds to results presented in Merchant (2006, 2012). The impact of the thermal deformation on translation and rotation differ over time, but the variation of rotation remains insignificant (less than 0.02 px/°C during acquisition). The thermal deformation is therefore reproducible and can be modeled and corrected. Further investigations are required to study the long term stability.

The experiments with the bundle block adjustment and spatial resection confirm the repeatability of the thermal impact on focal length using a different technique than image matching, and independent datasets. The same tendency for focal length expansion is observed (0.5 µm /°C) when the image sensor undergoes a temperature increase.

With terrestrial and aerial dataset, a better photogrammetric accuracy is achieved when taking the image sensor thermal effect into account. For the terrestrial dataset, the photogrammetric accuracy is improved by 1.5 times in standard acquisition configuration. To quantify the *bending effect*, a loop

closing error is examined (also referred to as GCP-free evaluation). This approach shows that by taking into account the thermal deformation, the *bending effect* is decreased by a factor of 3.6. For the aerial dataset in a linear configuration, an accuracy gain by a factor of 1.4 is observed.

7. Further Work

For the modeling with the bundle block adjustment and spatial resection experiment, the number of datasets remains insufficient and more datasets should be carried out so as to study thoroughly the issue. The variation of principal point is not reproducible, further investigations are required to better understand the problem.

Additionally, one should also focus on studies of the long term stability of the thermal effect. Although the reproducibility on the focal parameter has been verified thanks to dataset 3 of section 4.2 acquired 4 months after the first ones, we cannot yet be conclusive about the stability of the thermal deformation over time.

Nevertheless, even if a calibration is required at a regular basis, our calibration method based on 2D matching is simple to implement and fully automated. A possible limiting factor of the calibration strategy is the determination of interior parameters in a close range configuration and its use in aerial configurations Lichti et al. (2008).

In the meanwhile, we observed an improvement of accuracy for an airborne dataset (Section 5.2) and the thermal effect seems, at the first order, independent of the variation of interior parameters. We can summarize our suggestion as follows :

$$\begin{aligned} \mathscr{C}(T,d) =& \mathscr{C}(T_0,d) + \frac{\partial \mathscr{C}_{(T_0,d)}}{\partial T}\delta T \\ =& \mathscr{C}(T_0,d) + \frac{\partial \mathscr{C}_{(T_0,d_0)}}{\partial T}\delta T + \frac{\partial^2 \mathscr{C}_{(T_0,d_0)}}{\partial T \partial d}\delta T \delta d \end{aligned} \tag{6}$$

where : $\mathscr{C}(T,d)$ is a correction function depending on temperature T and field depth d ;
T_0 is the reference temperature ;
d_0 is the field depth for calibration

The 2nd order term $\frac{\partial^2 \mathscr{C}_{(T_0,d_0)}}{\partial T \partial d}\delta T \delta d$ can be considered negligible and the correction function can be expressed as :

$$\mathscr{C}(T,d) = \mathscr{C}(T_0,d) + \frac{\partial \mathscr{C}_{(T_0,d_0)}}{\partial T}\delta T \tag{7}$$

Under this assumption, the in-lab close-range calibration procedure is still valid even at considerable aerial operating distances.

Finally, experiences should be carried out with different image sensors to better study this phenomena.

Acknowledgements

We wish to thank the LOEMI team of the LaSTIG laboratory for all their help and in particular for providing the equipment. We thank Mathieu Peyréga for the loan of the Peltier thermoelectric cooler. Finally, we thank SIXENSE Mapping, Compagnie Nationale du Rhône and IGN companies for funding this research.

Références

Arya, S., Mount, D. M., Netanyahu, N. S., Silverman, R., and Wu, A. Y. (1998). An optimal algorithm for approximate nearest neighbor searching fixed dimensions. *J. ACM*, 45(6) :891–923.

Audi, A., Pierrot-Deseilligny, M., Meynard, C., and Thom, C. (2017). Implementation of an IMU aided image stacking algorithm in a digital camera for unmanned aerial vehicles. *Sensors*, 17(7).

CMOSIS (2013). *Application note for CMV - Temperature Sensor Calibration*, 2.1 edition.

CMOSIS (2015). *20 Megapixel global shutter CMOS image sensor - Datasheet*, 01 edition.

Daakir, M., Pierrot-Deseilligny, M., Bosser, P., Pichard, F., Thom, C., Rabot, Y., and Martin, O. (2017). Lightweight UAV with on-board photogrammetry and single-frequency gps positioning for metrology applications. *ISPRS Journal of Photogrammetry and Remote Sensing*, 127 :115 – 126. Geospatial Week 2015.

Fiedler, D. and Müller, H. (2013). *Impact of Thermal and Environmental Conditions on the Kinect Sensor*, pages 21–31. Springer Berlin Heidelberg, Berlin, Heidelberg.

Francois, G. and Yannick, G. (2017). The senseFly S.O.D.A. genesis. Presented at UAV Metric Camera Special Sessions DGPF Annual Meeting 2017 - Würzburg, Germany.

Fraser, C. S. (1997). Digital camera self-calibration. *ISPRS Journal of Photogrammetry and Remote sensing*, 52(4) :149–159.

Hirschmuller, H. (2008). Stereo processing by semiglobal matching and mutual information. *IEEE Transactions on Pattern Analysis and Machine Intelligence*, 30(2) :328–341.

Hothmer, J. (1958). Possibilities and limitations for elimination of distortion in aerial photographs. *The Photogrammetric Record*, 2(12) :426–445.

James, M. R. and Robson, S. (2014). Mitigating systematic error in topographic models derived from UAV and ground-based image networks. *Earth Surface Processes and Landforms*, 39(10) :1413–1420.

Kölbl, O. R. (1976). Metric or non-metric cameras. *Photogrammetric Engineering and Remote Sensing*, 42(1) :103–113.

Kraft, T., Gessner, M., Meißner, H., Cramer, M., Przybilla, H.-J., Gerke, M., et al. (2016). Evaluation of a metric camera system tailored for high precision UAV applications. *International Archives of the Photogrammetry, Remote Sensing and Spatial Information Sciences-ISPRS Archives*.

Kraft, T., Meißner, H., Berger, R., and Stebner, K. (2017). Preliminary results of developing a metric aerial camera for UAV applications. Presented at UAV Metric Camera Special Sessions DGPF Annual Meeting 2017 - Würzburg, Germany.

Lichti, D., Skaloud, J., and Schaer, P. (2008). On the calibration strategy of medium format cameras for direct georeferencing. In *International Calibration and Orientation Workshop EuroCOW*, number TOPO-PRESENTATION-2008-001.

Lin, D.-L., Wang, C.-C., and Wei, C.-L. (2010). Quantified temperature effect in a CMOS image sensor. *IEEE Transactions on Electron Devices*, 57(2) :422–428.

Lowe, D. G. (2004). Distinctive image features from scale-invariant keypoints. *International Journal of Computer Vision*, 60(2) :91–110.

Luhmann, T. (2010). Close range photogrammetry for industrial applications. *ISPRS Journal of Photogrammetry and Remote Sensing*, 65(6) :558 – 569. ISPRS Centenary Celebration Issue.

Maas, H.-G. and Hampel, U. (2006). Photogrammetric techniques in civil engineering material testing and structure monitoring. *Photogrammetric Engineering & Remote Sensing*, 72(1) :39–45.

Martin, O., Meynard, C., Pierrot-Deseilligny, M., Souchon, J., and Thom, C. (2014). Réalisation d'une caméra photogrammétrique ultralégère et de haute résolution. `https://drone.teledetection.fr/articles/Souchon_CAMLIGHT_IGN_rev.pdf`. (Accessed 07 December, 2016).

Mcglone, C., Mikhail, E., and Bethel, J. (1980). *Manual of Photogrammetry*. American Society of Photogrammetry, 5th edition.

Merchant, D. C. (2006). Influence of temperature on focal length for the airborne camera. In *Proc. of MAPPS/ASPRS Fall Conference*.

Merchant, D. C. (2012). Aerial camera metric calibration - history and status. In *Proceedings of ASPRS 2012 Annual Conference, Sacramento, Calif.*

Nex, F. and Remondino, F. (2014). UAV for 3d mapping applications : a review. *Applied Geomatics*, 6(1) :1–15.

Nocerino, E., Menna, F., and Remondino, F. (2014). Accuracy of typical photogrammetric networks in cultural heritage 3d modeling projects. *The International Archives of Photogrammetry, Remote Sensing and Spatial Information Sciences*, 40(5) :465.

Pan, B., Shi, W., and Lubineau, G. (2015). Effect of camera temperature variations on stereo-digital image correlation measurements. *Applied optics*, 54(34) :10089–10095.

Pauly, K., Aumont, J.-F., and Mancini, B. (2017). From off-the-shelf to off-the-charts : shifting the camera paradigm in commercial fixed wing UAS to increase accuracy. Presented at UAV Metric Camera Special Sessions DGPF Annual Meeting 2017 - Würzburg, Germany.

Pierrot-Deseilligny, M. and Clery, I. (2011). Apero, an open source bundle adjusment software for automatic calibration and orientation of set of images. *ISPRS - International Archives of the Photogrammetry, Remote Sensing and Spatial Information Sciences*, XXXVIII-5/W16 :269–276.

Pierrot-Deseilligny, M. and Paparoditis, N. (2006). A multiresolution and optimization-based image matching approach : An application to surface reconstruction from SPOT5-HRS stereo imagery. *Archives of*

Photogrammetry, Remote Sensing and Spatial Information Sciences, 36(1/W41).

Remondino, F. and Fraser, C. (2006). Digital camera calibration methods : considerations and comparisons. *International Archives of Photogrammetry, Remote Sensing and Spatial Information Sciences*, 36(5) :266–272.

Rieke-Zapp, D. H. and Nearing, M. A. (2005). Digital close range photogrammetry for measurement of soil erosion. *The Photogrammetric Record*, 20(109) :69–87.

Rosu, A.-M., Pierrot-Deseilligny, M., Delorme, A., Binet, R., and Klinger, Y. (2015). Measurement of ground displacement from optical satellite image correlation using the free open-source software MicMac. *ISPRS Journal of Photogrammetry and Remote Sensing*, 100 :48 – 59. High-Resolution Earth Imaging for Geospatial Information.

Rupnik, E., Daakir, M., and Pierrot Deseilligny, M. (2017). MicMac – a free, open-source solution for photogrammetry. *Open Geospatial Data, Software and Standards*, 2(1) :14.

Saks, N. (1980). A technique for suppressing dark current generated by interface states in buried channel CCD imagers. *IEEE Electron Device Letters*, 1(7) :131–133.

Sauer, D. J. (2001). CMOS image sensor with reduced fixed pattern noise. US Patent 6,320,616.

Schwartz, J. (2010). New CMOS image sensor is useful in extreme temperatures.

Smith, M. and Cope, E. (2010). The effects of temperature variation on single-lens-reflex digital camera calibration parameters. *International Archives of Photogrammetry, Remote Sensing and Spatial Information Sciences*, 38(Part 5).

Tournadre, V. (2015). *Métrologie par photogrammétrie aéroportée légère : application au suivi d'évolution de digues*. PhD thesis, Université Paris-Est. Thèse de doctorat dirigée par Pierrot-Deseilligny, Marc Signal, Image, Automatique Paris Est 2015.

Triggs, B., McLauchlan, P. F., Hartley, R. I., and Fitzgibbon, A. W. (1999). Bundle adjustment - a modern synthesis. In *International workshop on vision algorithms*, pages 298–372. Springer.

Vallet, J. (2007). GPS/IMU and LiDAR integration to aerial photogrammetry : Development and practical experiences with Helimap system. *Vorträge Dreiländertagung*, 27.

Widenhorn, R., Blouke, M. M., Weber, A., Rest, A., and Bodegom, E. (2002). Temperature dependence of dark current in a CCD. In *Sensors and Camera Systems for Scientific, Industrial, and Digital Photography Applications III*, volume 4669, pages 193–202. International Society for Optics and Photonics.

Yastikli, N. and Jacobsen, K. (2005). Influence of system calibration on direct sensor orientation. *Photogrammetric Engineering & Remote Sensing*, 71(5) :629–633.

Zhou, Y., Rupnik, E., Faure, P.-H., and Pierrot-Deseilligny, M. (2018). GNSS-assisted integrated sensor orientation with sensor pre-calibration for accurate corridor mapping. *Sensors*, 18(9).